COMMUNICATION

ADVANCED
MATERIALS
www.advmat.d[...]

Check for
updates

Bioinspired Anti-Plateau–Rayleigh-Instability on Dual Parallel Fibers

Pengwei Wang, Jiajia Zhou, Bojie Xu, Cong Lu, Qing'an Meng, and Huan Liu*

The Plateau–Rayleigh instability (PRI) is a well-known phenomenon where a liquid column always breaks up into droplets to achieve the minimization of surface energy. It normally leads to the non-uniformity of a liquid film, which, however, is unfavorable for the fluid coating process. So far, strategies to overcome this instability rely on either the surfactants, UV/high-temp curing treatments, or specific chemical reactions, which suffer from both limited liquid composition and complicated experimental conditions. Natural mulberry silk, a typical composite fiber, is produced by silkworms through a similar fluidic coating process, but exhibits a remarkably uniform and smooth surface. Drawing inspiration, it is revealed that the unique dual parallel fibers are capable of overcoming the PRI during the fluid coating process. Such anti-PRI ability is attributable to the changes in the Laplace pressure difference caused by the alternative asymmetry of the liquid film, as has been demonstrated by both a force analysis on the irregular liquid film and theoretical simulation according to the stability of the liquid on parallel fibers in the fluid coating process. The strategy is applicable for preparing various smooth functional coatings on fibers, which offers new perspectives for fluid coating and microfluidic technologies.

The Plateau–Rayleigh instability (PRI) is a well-known phenomenon where a liquid column always breaks up into spherical droplets to achieve minimization of the surface energy.[1] This common phenomenon is called PRI, also known as the capillary instability, which has been utilized in making both the ordered droplets and the periodic fibrous structures in versatile applications, such as inkjet printing,[2] microfluidics,[3] spindle knots fibers,[4] and cell microcarrier arrays.[5] However, sometimes the uneven liquid film brought by the PRI is disadvantageous for the fabrication of composite fibers by techniques of fluid coating, electrospinning, and microfluidics.[6] Previous

studies demonstrated that the space confinement could suppress the PRI.[7] It was essentially performed in a sandwiched half-close system at certain operating conditions (the high temperature), which is difficult to apply to various liquids and open systems.[7] Recently, the capillary force-induced fibrous coalescence was also reported, where the liquid spreading was facilitated with two fibers approaching to each other and consequently forming a uniform liquid column.[8,9] In these cases, the amount of liquid per unit length on fibers, a key factor for the appearance of the PRI, is limited and decreases with the liquid spreading, and therefore is not enough to cause the PRI. So far, the most frequent approach for overcoming the PRI depends on either the surfactants, the UV/hi-temp curing treatments or specific chemical reactions, and these strategies normally suffer from both the limited liquid composition and the waste of energy resources.[10] Thus, proposing a simple and general strategy to overcome the PRI in a fibrous fluid coating process under the mild condition is in demand.

Mulberry silk, one of the earliest natural animal fibers used by humans, has received significant attention due to the unique smooth surface, extreme strength, and commendable hypoallergenicity.[11] When spun out from the spinneret of the silkworm, the silk exhibits a composite structure where outer liquefied sericin fully encloses the inner fibroin fibers.[12] One remarkable observation is that the solidified mulberry silk is extremely uniform and smooth, and the PRI seems not to take place during the spinning period.

In this work, inspired by the unique structure of the mulberry silk, we developed a simple anti-PRI strategy by using dual cylindric fibers with a side-by-side parallel arrangement, which proceeds in a mild atmospheric room temperature condition and free from any additional post-treatment. It is proposed that the change in the Laplace pressure difference caused by the alternative asymmetry of the liquid film plays a key role in overcoming the PRI. Based on the linear stability analysis and the estimation of the liquid amount during the coating process, we conducted a theoretical calculation to predict the stability of the liquid film on dual parallel fibers, where the model is based on the experimental relevant parameters such as the liquid viscosity and the pulling speed. Using such facile strategy, direct coating of homogeneous and smooth film on

Dr. P. Wang, Prof. J. Zhou, Dr. B. Xu, C. Lu, Dr. Q. Meng,
Prof. H. Liu
Key Laboratory of Bio-Inspired Smart Interfacial Science
and Technology of Ministry of Education
School of Chemistry
Beijing Advanced Innovation Center for Biomedical Engineering
International Research Institute for Multidisciplinary Science
Beihang University
No. 37, Xueyuan Road, Haidian District, Beijing 100191, P.R. China
E-mail: liuh@buaa.edu.cn

The ORCID identification number(s) for the author(s) of this article
can be found under https://doi.org/10.1002/adma.202003453.

**ADVANCED
SCIENCE NEWS**

www.advancedsciencenews.com
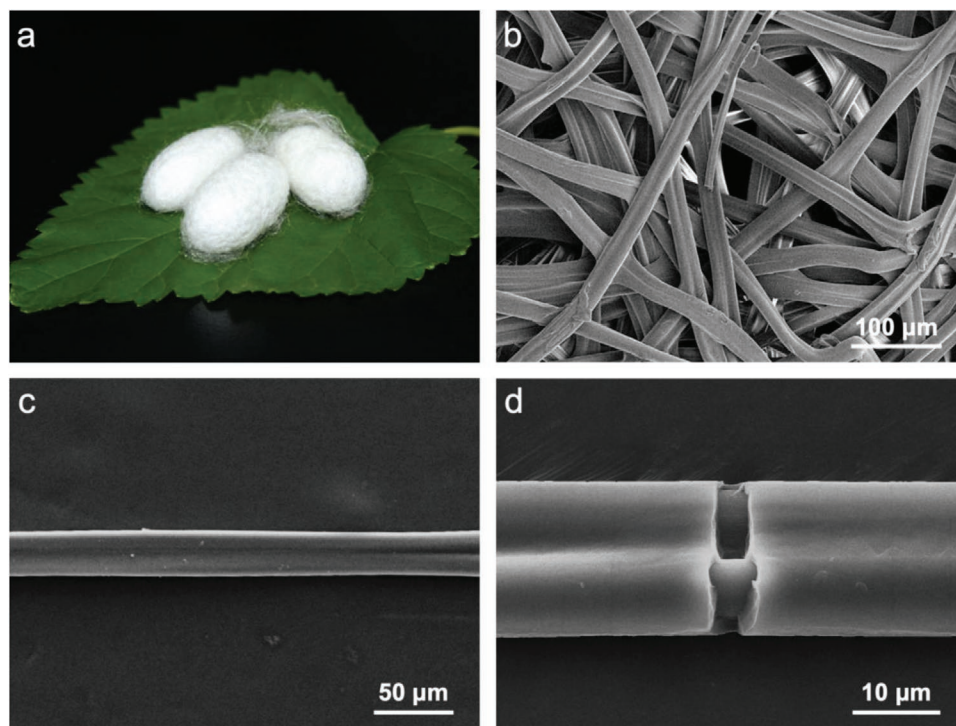
**ADVANCED
MATERIALS**

www.advmat.de

Figure 1. The morphologies of the mulberry cocoon and silk. a) Optical picture of the cocoon. b) SEM image of the surface of the cocoon, showing typical fibrous network structures. c) SEM image of a complete mulberry silk, showing smooth and uniform surface. d) SEM image of a broken mulberry silk with partial fibroin fibers exposed, showing the composite structure of the inner dual parallel solid fibers with a smooth surface coating.

fibers with various liquids was realized under mild conditions. We envision that this anti-PRI strategy offers new perspectives for the fibrous fluid coating and microfluidic technologies.

Figure 1a shows the optical picture of the cocoon made of mulberry silks. The scanning electron microscopy (SEM) image reveals that the mulberry silks are interlaced on the cocoon surface, showing network structural characteristics in which the intersections are bonded by sericin coating (Figure 1b). As a protective covering for the pupa, though with extremely thin thickness and light weight, the cocoon is difficult to tear due to the high strength adhesion between silks, which is guaranteed by the completeness and uniformity of the sericin coating. Of note is that the silk on cocoon surface exhibits a ribbon structure with a complete and smooth exterior (Figure 1c), differing from the spindle-knotted structure of the spider silk.[13] It suggests that a rather homogeneous sericin coating was enabled during the mulberry silk spinning process. Thus, to explore the reason for this anti-PRI phenomenon, we characterized the inner structure of the mulberry silk. As shown in Figure 1d, the scanning electron microscopy (SEM) image of a broken mulberry silk with partially exposed fibroin fibers reveals that the mulberry silk has a unique two-tier composite structure in which the sericin coating closely surrounds dual parallel fibroin fibers ($\approx$8 to 10 μm in diameter). Taken together, the silkworm refrains from the occurrence of the PRI during the silk spinning process, where the special parallel arrangement of the fibroin fibers may play a key role.

To be noticed, the mulberry silk is drawn out from the spinneret of the silkworm.[14] Therefore, a similar fluid coating method was employed to explore the anti-PRI capability of the

dual parallel fibers. The single circular nylon fiber ($\approx$130 μm in diameter, Figure S1, Supporting Information) and the dual parallel nylon fibers ($\approx$130 μm in diameter) were horizontally pulled out from a reservoir of silicone oil (96.5 mPa s) through a capillary tube (inner diameter of $\approx$500 μm) by a manipulator at a velocity of 1 cm s^{-1} in order to avoid gravity-induced liquid flow. The processes were recorded in situ by a charge coupled device (CCD) camera where the evolution of the liquid film on the single, and the dual parallel nylon fibers was shown in **Figure 2**a,b respectively. Particularly, liquid spreading on the fiber cannot proceed freely in this fluidic coating process, which makes the amount of liquid per unit length of fiber big enough to cause PRI. When the single fiber was drawn out of the reservoir, uniform silicone oil film was formed at the very beginning (0 s, Figure 2a). Then, the liquid film became unstable initialized by a small external perturbation,[1] which eventually led periodic regions of the liquid film to grow thinner or thicker continuously from 0.3 s to 0.9 s. During this process, the Laplace pressures are different in regions of different thickness, caused by the difference in the radius of the curvature. The difference in Laplace pressure then promoted the growth of instability, eventually leading to the formation of periodic droplets on the single fiber ($\approx$1.5 s, Figure 2a). In comparison, the situation was dramatically different for the dual parallel fibers. When dual parallel fibers were drawn out from the liquid reservoir under the same experimental condition, the silicone oil film remained uniform and stable on the parallel fibers without breaking up for an extremely long time (>50 s, Figure 2b). It clearly demonstrates that the parallel arrangement of dual fibers can effectively overcome the PRI.

**ADVANCED
SCIENCE NEWS**

www.advancedsciencenews.com

**ADVANCED
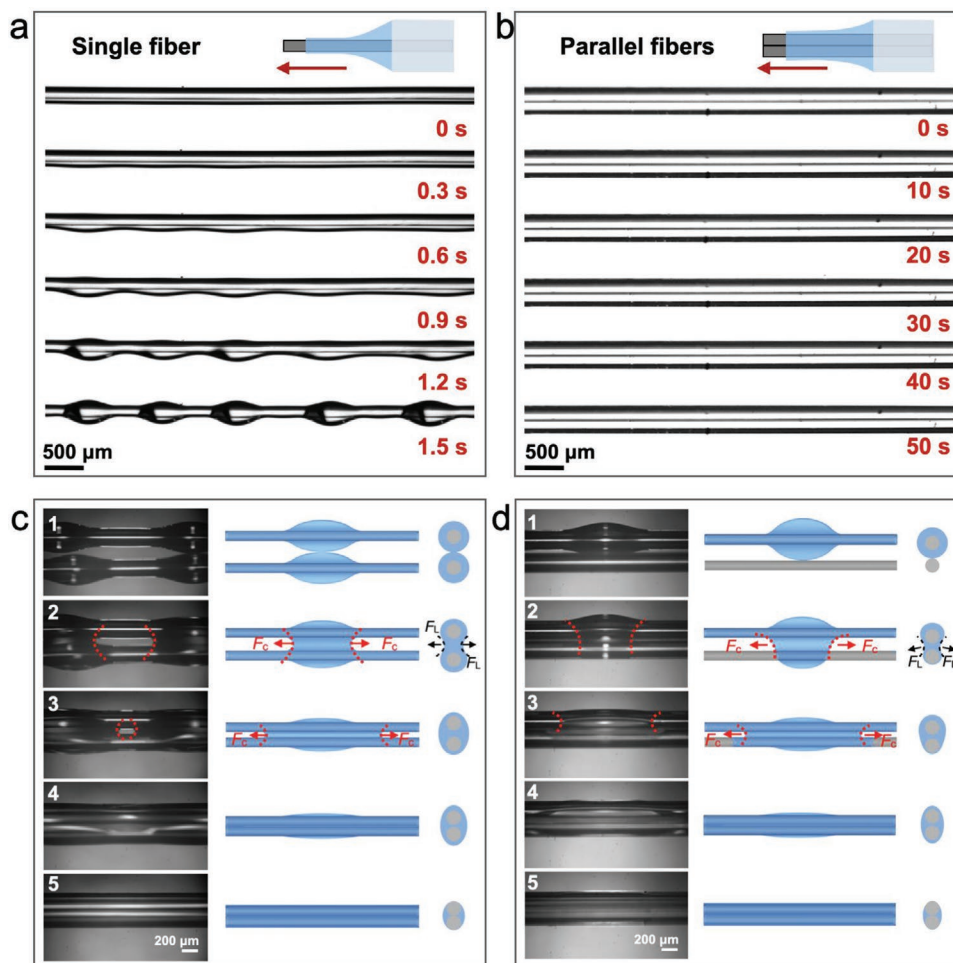MATERIALS**

www.advmat.de

Figure 2. In situ observation of the anti-PRI behavior on the dual parallel fibers. a,b) Optical pictures of the fluid coating process of a single nylon fiber and the dual parallel nylon fibers, respectively. a) For a single fiber, the liquid film breaks up into periodic droplets in 1.5 s, showing a typical PRI behavior. b) For the dual parallel fibers, the liquid film remains homogeneous and smooth for over 50 s, showing an anti-PRI behavior. c) The dynamic approaching process of two fibers encapsulated with periodic droplets, where the periodic droplets gradually disappear and become a smooth liquid film. The liquid amount on per unit length of the fiber remains unchangeable. d) The dynamic approaching process of a dry fiber and a wet fiber encapsulated with periodic droplets, by which the periodic droplets on the wet fiber gradually become a smooth liquid film. The liquid amount on per unit length of the fiber decreases with time.

The anti-PRI ability of the dual parallel fibers was further confirmed by a different experimental protocol, where the dynamics of the liquid film on the fibers were characterized by using cylindrical glass fibers (≈ 300 μm in diameter) and silicone oil (96.5 mPa s). First, two single glass fibers with periodic droplets were prepared through a dip coating method based on the typical PRI behavior (Figure 2c$_1$), as has been extensively studied.[4] Then these two wet fibers approached each other gradually (Figure 2c). When the droplets on adjacent fibers came into contact with each other, the liquid immediately spread between two fibers (Figure 2c$_2$–c$_4$). Consequently, periodic droplets were eliminated, forming a rather uniform coating when two fibers came into contact with each other in parallel (Figure 2c$_5$). As indicated by the schematic cartoons, the liquid spreading caused by the fibrous approaching was attributable to the synergetic effect of two driving forces: one is the capillary force F_C along the corner between two fibers, originating from the interfacial energy gain when liquid spreads in

a cornered region;[15–17] the other is the Laplace force F_L, which drives the liquid to the conformation with a lesser surface area. A similar result could be observed in another condition where the periodic droplets on adjacent fibers were staggered artificially (Figure S2, Supporting Information). Worth noting is that the amount of liquid on fibers remained unchanged during the whole process. While the liquid film is unstable on individual fibers, the same amount of liquid distributed on dual-fiber setup led to a stable configuration. Therefore, the anti-PRI behavior was clearly shown, which can be further confirmed by the long-time stability of the uniform liquid film on closely attached dual fibers (Figure 2c$_5$). On the other hand, when a dry glass fiber is pushed to approach a wet fiber with periodic droplets, the liquid rapidly enveloped the dry fiber and spread along the gap of the two fibers when the droplets came into contact with the dry fiber (Figure 2d$_1$–d$_4$). In this process, droplets on wet fiber dwindled in size and finally disappeared, forming a stable liquid film (Figure 2d$_5$), that is, the PRI was effectively

eliminated. Similarly, both F_C and F_L play significant roles in driving the liquid to spread on the parallel fibers. In this case, the liquid amount on per unit length of the fiber decreases with time in certain degree due to the introducing of another dry fiber, which differs from the spreading of a single liquid droplet on two fibers.[8] Taken together, the results indicate that even happening on a single fiber, the PRI can be overcome shortly by introducing another parallel fiber, suggesting the anti-PRI ability for the dual parallel fibers.

To explore the dynamic behavior of the liquid film on both a single fiber and the dual parallel fibers, force analyzing was

conducted. For a single fiber, the PRI of the liquid film always happened (**Figure 3**a), caused by the existence of tiny perturbations in the stream.[1] As time progresses, the perturbations in the liquid film will be resolved into sinusoidal components (wave): the growing components (the peak) shows a bigger radius of curvature (R_p) comparing that of the decaying components (R_t at the trough) in the transverse section, namely, $R_p > R_t$ (Figure 3a). Thus, the Laplace pressure pointing to the circle center at the peak (F_{R-p}) is smaller than that at the trough (F_{R-t}), namely, $F_{R-p} < F_{R-t}$. As a result, the as-generated Laplace pressure difference (F_R) drives the liquid moving from
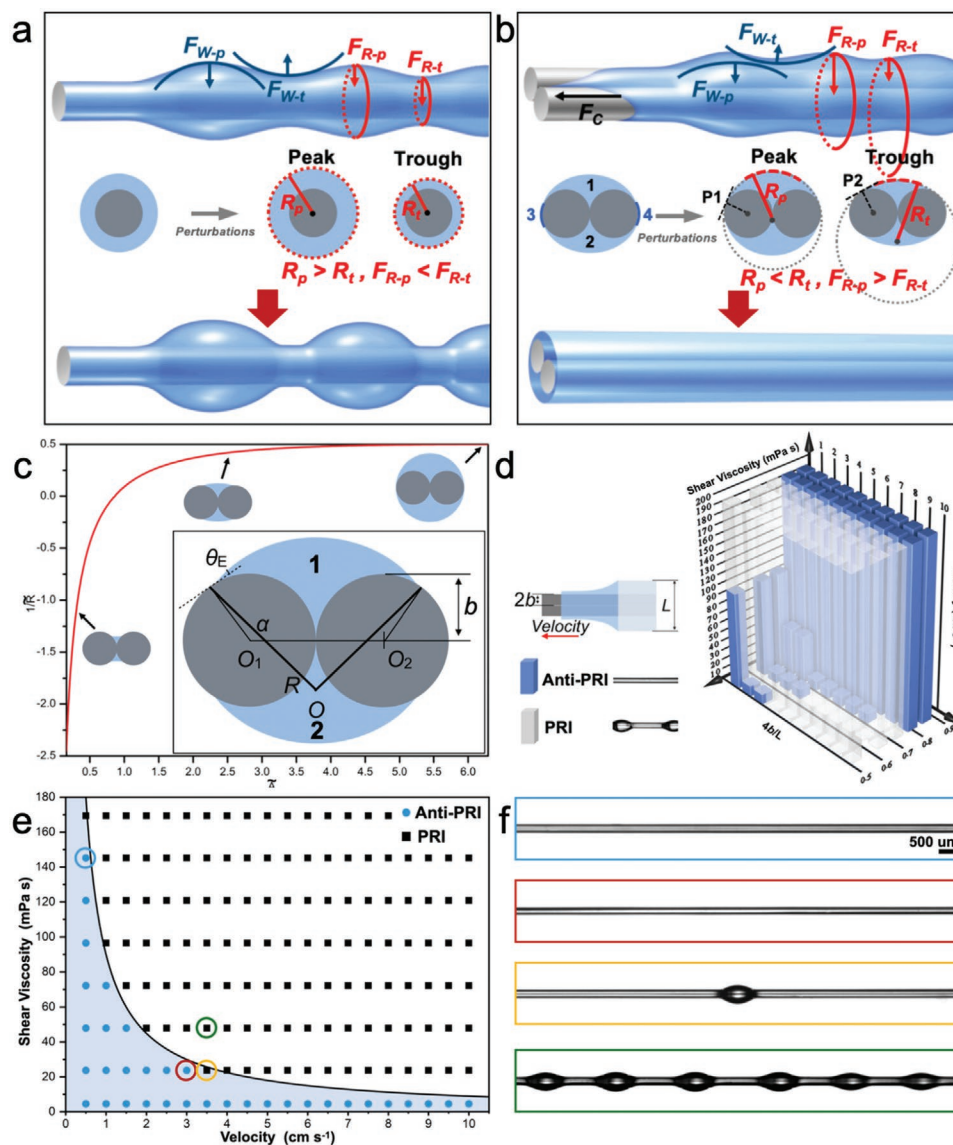

Figure 3. Theoretical analysis of the liquid film stability. a,b) Force analysis of the stability of the liquid film on a single fiber and the dual parallel fibers, respectively. a) For a single fiber, the perturbations in the liquid film become periodic droplets under the cooperative effect of F_w and F_R, that is, the Laplace pressure differences on different directions. b) For the dual parallel fibers, the perturbations in the liquid film die down by the changes of the effect of F_w and F_R, and also the F_c between fibers. c) The relationship between the sectional shape and the quantity of the liquid on the parallel fibers. d) 3D map shows the relationship between the pulling velocity of the dual parallel fibers, the shear viscosity of the silicone oils and the diameter ratio of the double diameter of the fiber to the internal diameter of the capillary tube (blue column: the anti-PRI regime; gray column: the PRI regime). e) Phase diagram of the PRI behavior depending on the viscosity and the velocity when the dual parallel fibers with ≈100 μm diameter was pulled out from the capillary glass tube with ≈500 μm inner diameter. f) Optical images of the final states of the liquid film on the dual parallel fibers under corresponding experimental conditions indicated in Figure 3e

the trough to the peak, which further aggravates this instability. Meanwhile, another radius component is the radius of curvature of the wave itself (blue arcs, Figure 3a), and the as-generated Laplace pressure difference (F_W) is liable to weaken this instability. On a single cylindrical fiber, F_R and F_W act oppositely, and the F_R acts dominantly, leading to the exponential growth in the sinusoidal components with time. Consequently, the liquid film breaks into periodic droplets, and the PRI happens (Figure S3, Supporting Information). In this process, the surface tensions, tending to minimize the surface area of the liquid film, play a critical role.

However, the situation is different for the dual parallel fibers. For the liquid film on the dual parallel fibers (Figure 3b), the cross section gives a non-circle irregular shape composed of two separated partial-circles on the wide sides (Part 1 and 2, Figure 3b) that might be connected by microscale thin liquid films on the narrow sides (Part 3 and 4, Figure 3b). Here, two partial-circles are aroused by the unique non-circle cross-sectional topology, resembling the liquid film on an elliptical wire.[18] Worth noting is the microscale smooth liquid films on the narrow sides (Part 3 and 4, Figure 3b, which is attributable to the intermolecular van der Waals forces between solid and liquid.[19–21] Such microscale liquid films play an important role for complete enclosing of the fibers by liquid, as has been directly evidenced by the uniform and intact polymer coating on fibers that are mentioned later. Such non-circle cross-sectional topology drastically altered the local curvatures comparing with that on a single cylindrical fiber. In case of small perturbations, the cross section of the liquid film at the trough tends to show a larger radius of curvature than that of the peak ($R_p < R_t$), imparted by the structural effect of the dual parallel fibers. The as-generated Laplace pressure pointing to the circle center at the peak (F_{R-p}) is greater than that at the trough (F_{R-t}), namely, $F_{R-p} > F_{R-t}$. Thus, the F_R promotes the restoration of the uniformity of the liquid film. The F_W caused by the radius of curvature of the wave itself is also helpful for resisting the fluctuations. On parallel fibers, both effects (F_R and F_W) simultaneously promote the repair of perturbations, thereby overcoming the occurrence of the PRI. Meanwhile, the wedge shaped corner between parallel fibers offers a F_C at the end of the liquid film to facilitate the liquid spreading along the long axis direction,[8] which is helpful for overcoming the fluidic instability on fibers[22] especially at the beginning when fibers were pulled out from the liquid reservoir (Figure 2c,d).

To explore the stability criterion of the liquid on dual fibers,[4,9,23] we performed a linear stability analysis of the liquid film on the dual-fiber setup (Figure S4, Supporting Information). To be noticed, the fibrous coating process we used differs from the systems with limited amounts of liquid on fibers, where the stability of the liquid was analyzed based on minimizing the total interfacial energy.[23,24] First, we derive the relationship between the meniscus shape and the quantity of the liquid. With increasing the liquid quantity, the cross section of the liquid film on parallel fibers changes from two separated partial-circles to one full circle, as shown in Figure 3c in which b is the radius of the fiber, θ_E is the liquid–fiber contact angle, α is the wrapping angle, R is the radius of curvature, and A is the cross-sectional area of the liquid film that is mainly composed of the part 1 and 2 (Figure 3c). We will use dimensionless

quantities by scaling the length with the fiber radius b and the area with b^2. In experiments, the two fibers were in contact and the liquid fully wets the fiber ($\theta_E = 0°$). In this case, we have the following expressions for the dimensionless radius of curvature and the cross-section area,

$$\frac{1}{\tilde{R}} = -\frac{\cos\alpha}{1 - \cos\alpha} \tag{1}$$

$$\tilde{A} = 4(1 - \cos\alpha)\sin\alpha - 2(\alpha - \sin\alpha\cos\alpha) \\ - 2\tilde{R}^2\left(\frac{\pi}{2} - \alpha - \sin\alpha\cos\alpha\right) \tag{2}$$

Here $1/R$ and A are related through the wrapping angle α. We plotted $1/R$ as a function of A in Figure 3c in which when $\alpha = \pi$, $1/R = 1/2$ and $A = 2\pi$. When $A > 2\pi$, the liquid film completely packages the fibers; the relationship between $1/R$ and A can be written as:

$$\frac{1}{\tilde{R}} = \sqrt{\frac{1}{\frac{\pi}{\tilde{A}} + 2}}. \tag{3}$$

For parallel-fibers, there is a critical amount of fluid that the two fibers can hold. Below this threshold, the fluid is stable; while above this threshold, the fluid becomes unstable. The linear stability analysis (see Supporting Information) indicates the critical amount corresponding to the fluid which can fully enclose the two fibers in a circle (for $\theta_E = 0°$): $2\pi b^2$.

To proceed, we need to know the amount of fluid covering the parallel fibers. The coating problem on a fiber with an irregular cross section is complicated and known results are based on simple geometries.[25] One example is the Landau–Levich–Derjaguin (LLD) model[26] for the coating on a planar surface. The thickness of the film is $e \propto \kappa^{-1} Ca^{2/3}$, where the characteristic length is the capillary length and $Ca = \eta V/\gamma$ is the capillary number (η is the shear viscosity, V is the pulling speed, and γ is the surface tension). The other example is the coating on a circular fiber,[25,27] $e \propto b\, Ca^{2/3}$, where the characteristic length is the fiber's radius b. Based on these classical models, we anticipate the $Ca^{2/3}$ scaling still holds for the irregular cross-section. The area of the fluid film in the cross-section is $A = k\, Ca^{2/3}$ where k is a geometric factor depending on the shape of the cross section. The critical amount of fluid corresponds to the following critical capillary number

$$Ca > Ca_{crit} = (2\pi b^2/k)^{3/2} \tag{4}$$

To test the analysis above, dual parallel nylon fibers with different diameters (Figure 3d, and Figure S6, Supporting Information) were pulled out horizontally from the silicone oil reservoir with different viscosities in different velocities through capillary glass tubes with different internal diameters. The results demonstrate that there is a PRI happening demarcation line, and it is noteworthy that the diameter ratio of the nylon fibers to the capillary glass tubes plays an essential role in anti-PRI by limiting the thickness of the liquid film (Figure S6c,f, Supporting Information). Thus, to avoid the influence of the

ADVANCED
SCIENCE NEWS
www.advancedsciencenews.com

ADVANCED
MATERIALS
www.advmat.de

diameter ratio, nylon fibers with 100 µm diameter and a capillary glass tube with 500 µm inner diameter were specifically employed. We confirmed that in lower velocity and viscosity conditions, the parallel fibers can effectively overcome the PRI (Figure 3e, the blue dots). The optical images of the stable states of the liquid film in different conditions are recorded in Figure S6, Supporting Informationand four representative situations were indicated by circles in Figure 3e and the corresponding stable liquid film states were shown in Figure 3f. In the anti-PRI regime, the homogeneous and smooth liquid films on fibers prepared at various conditions remain stable (Figure 3e,f, the blue and the red circles); in the PRI regime, with the increase of the quantity of liquid, that is, the velocity and the viscosity, the periodic droplets caused by the PRI appear and increase gradually (Figure 3e,f, the yellow and the green circles). For our experiment, the instability condition is
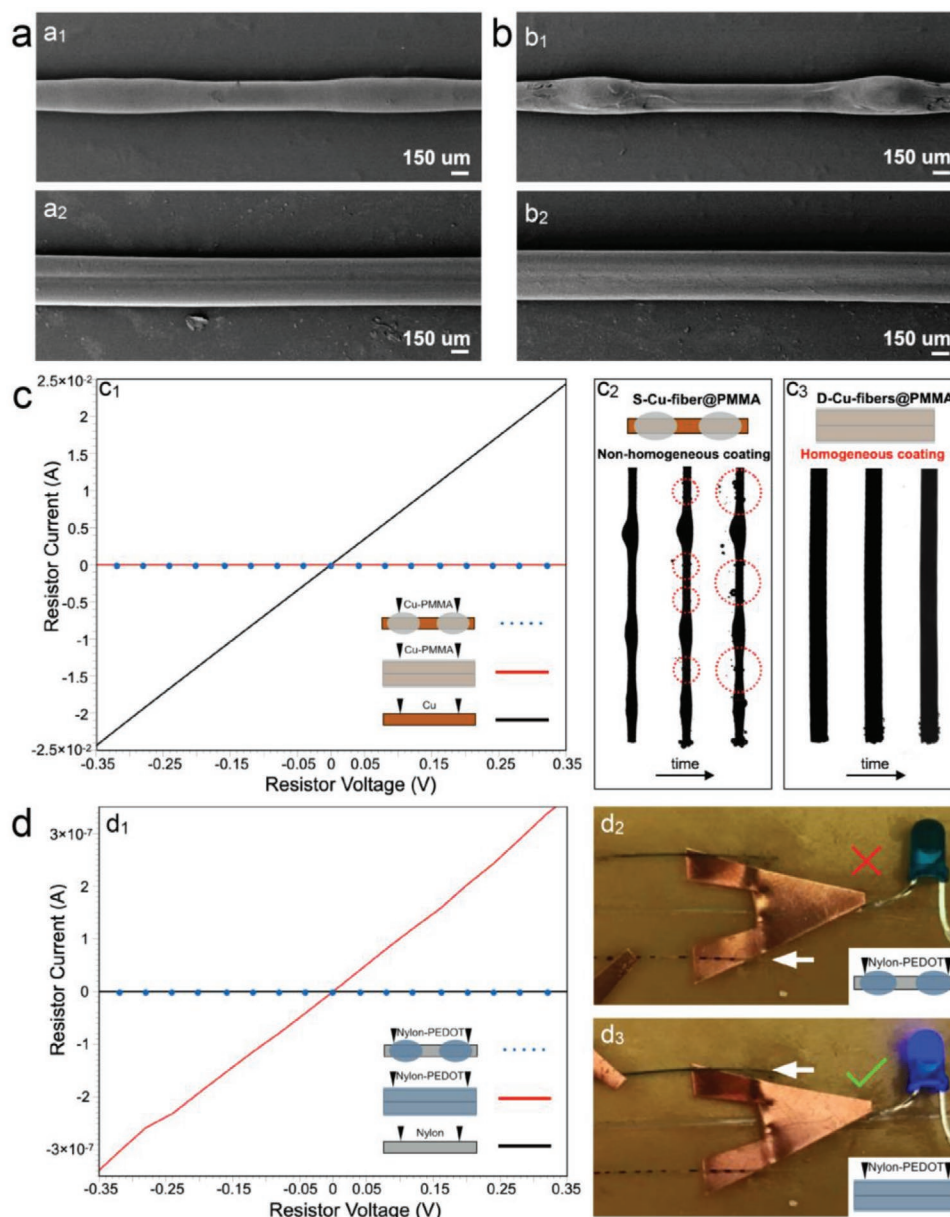

Figure 4. Fabrication of bioinspired functional fibers with homogeneous and smooth coatings. a,b) SEM images of a single (a_1,b_1) and dual (a_2,b_2) parallel nylon fibers with a PMMA-coating fabricated by fluid coating process at the velocity of 3 mm s^{-1} and 5 mm s^{-1}, respectively. c) The electrical measurement of PMMA-coated copper fibers. c_1) The I–V curves of a single copper fiber (black solid line), the S-Cu-fiber@PMMA (blue dots) and the D-Cu-fibers@PMMA (red solid line). c_2) The hydrogen bubbles generate on the S-Cu-fiber@PMMA when performing HER. Red dashed circles: hydrogen bubbles generate in between the periodic knots. c_3) There are no hydrogen bubbles generated on the D-Cu-fibers@PMMA in HER. d) The electrical measurement of PEDOT:PSS-coated nylon fibers. d_1) The I–V curves of the single nylon fiber (black solid line), the S-nylon-fiber@PEDOT:PSS (blue dots), and the D-nylon-fibers@PEDOT:PSS (red solid line). d_2) The LED goes out when connected with the S-nylon-fiber@PEDOT:PSS in a circuitry. d_3) The LED goes on when connected with the D-nylon-fibers@PEDOT:PSS in a circuitry.

found to be $\overline{\eta}\overline{V} > 90$, where the viscosity η is in unit of mPa s and velocity V in unit of cm s^{-1}. The surface tension of the silicone oil is about 19 mN m^{-1}. This leads to a critical capillary number, $Ca_{crit} \approx 0.05$ for the parallel-fiber geometry. When the experimental capillary number is greater than Ca_{crit}, the film is unstable and undergoes PRI (Figure 3e, the black dots). This provides an operational criterion for the selection of the fluid and experimental parameters.

Taking advantage of the anti-PRI capability of the dual parallel fibers, we fabricated various two-tier composite fibers with uniform coating by the fluid coating method without additional treatments. First, nylon fibers with a poly(methyl methacrylate) (PMMA) coating were fabricated by drawing the single and dual parallel nylon fibers in contact ($\approx$130 μm in diameter) out from polymer solution at the different velocity (3 mm s^{-1} in **Figure 4**a, 5 mm s^{-1} in Figure 4b). The polymer solution is composed of PMMA dissolving in *N,N*-dimethylformamide with a weight percentage of 13%. The SEM images of the as-prepared PMMA-coated single fibers (S-fiber@PMMA) in Figure 4a$_1$,b$_1$ both show apparent periodic knots. Specifically, larger periodic knots could be observed in Figure 4b$_1$ because of the higher drawing velocity. In contrast, as illustrated in Figure 4a$_2$,b$_2$, the as-prepared PMMA-coated dual parallel fibers (D-fibers@PMMA) both exhibit uniform and smooth surface without periodic knots. The results demonstrate that in the fluid coating process, the parallel arrangement of dual fibers can prevent the PRI-induced damage on fiber surface without using traditional high-temp/UV curing treatments or specific chemical reactions, and then significantly expand the scope of the choice of coating materials. Moreover, conductive copper fibers with insulating PMMA coating and insulating nylon fibers with a conductive poly(3,4-ethylenedioxythiophene) polystyrene sulfonate (PEDOT:PSS) coating were both fabricated by a simple fluid coating method. Worth noting is the drastically different electrical properties for the case of the single and the dual fibers in contact, even prepared under the same condition, which were characterized by measuring the *I–V* curves. As shown in Figure 4c$_1$, although the single (blue dots) and the dual parallel (red line) copper fibers with PMMA coating both exhibit little electronic signals, they give essentially different electric behaviors when used as working electrodes in hydrogen evolution reaction (HER). The single copper fiber with PMMA coating (S-Cu-fiber@PMMA) shows apparent electrical leakage phenomenon, where tiny bubbles generate between the periodic knots on the single fiber (Figure 4c$_2$). In contrast, hydrogen bubbles can only generate on the incision of the PMMA-coated dual parallel copper fibers (D-Cu-fibers@PMMA) (Figure 4c$_3$), indicating the formation of a homogeneous full-coverage PMMA coating. Meanwhile, we measured the electrical conductivity of the PEDOT:PSS-coated nylon fibers (Figure 4d$_1$). Dual parallel nylon fibers with PEDOT:PSS coating (D-nylon-fibers@PEDOT:PSS) exhibit excellent electrical conductivity, demonstrating the completeness of the PEDOT:PSS film (Figure 4d$_1$, red line). However, the PEDOT:PSS-coated single nylon fiber (S-nylon-fiber@PEDOT:PSS) is electrical insulating (Figure 4d$_1$, blue dots), illustrating that the PEDOT:PSS film on single nylon fiber breaks because of the PRI. This result was further confirmed by constructing circuitry with a LED (Figure 4d$_2$,d$_3$), which went on when connecting the D-nylon-fibers@PEDOT:PSS and went out when combining the S-nylon-fiber@PEDOT:PSS. Taken together, by constructing a parallel arrangement of dual fibers, uniform coatings with excellent electrical insulation or conductivity on fibers were fabricated directly, indicating that the anti-PRI capability of the parallel fibers can be sufficiently flexible for a wide range of applications.

In conclusion, inspired by the unique inner structure of the mulberry silk, we developed a simple approach to overcome the PRI on fibers, which avoids complicated treatments and the limitation of the specific curing agents or coating materials. By observation of the inner structure of the mulberry silk, we revealed the relationship between the special parallel arrangement and the anti-PRI ability of the fibroin fibers. Further, through the stability analysis of the liquid film on dual parallel fibers, we established a theoretical model for fluid coating process, in which the fluid viscosity and fiber drawing speed determine whether the PRI happens or not on parallel fibers. Finally, we fabricated bioinspired smooth functional fibers by using the fluid coating method with different fibers and coating materials, proving the wide and flexible applicability of this method. We envision that this simple and effective anti-PRI approach will provide new perspectives for the fluid coating and microfluidic technologies.

Experimental Section

Characterization of the Mulberry Cocoon and Silk: The optical image of the cocoon was observed with a camera (D600, Canon, Japan). The microstructures of the cocoon were observed with a scanning electron microscope (JSM-7500F, JEOL, Japan). The microstructures of the broken mulberry silks were observed by an environmental scanning electron microscope (Quanta 250 FEG, FEI, USA).

Anti-PRI Behaviors in Fluid Coating Processes: The nylon fibers with ≈100 μm, 130 μm, 180 μm, and 200 μm in diameter were tightly fixed in the silicone oils reservoir through capillary tubes (≈300 and 500 μm in inner diameters), with the ends connected to a motor. The size of the solution container is 2 cm × 3 cm × 2 cm (width × length × height). When the motor is on, the fiber is stretched out and evenly coated with the silicone oils as it moves out of the reservoir. The process was recorded by a CCD (acA1600-60 gm, Basler, Germany).

Anti-PRI Behaviors in Fibers Approaching Processes: Dry glass rod (≈300 μm in diameter) was vertically pulled out from silicone oil (96.5 mPa s) at the speed of 1 cm s^{-1}. Then, the liquid film on the glass rod broke up into period droplets by the PRI. The rods approaching processes were carried out by a programmable mobile stage. The processes were recorded by a high-speed camera.

Fabrication of Bioinspired Functional Fibers: The polymer solution is composed of PMMA dissolving in *N,N*-dimethylformamide with a weight percentage of 13%. The concentration of PEDOT:PSS (with 0.8 wt% PEDOT and 0.5 wt% PSS) solution (5 wt% in water with the addition of 5 wt% dimethyl sulfoxide to enhance the conductivity) was obtained from Sigma-Aldrich. The electrical measurement of the PMMA-coated copper fibers and PEDOT:PSS-coated nylon fibers were characterized using a Keithley 4200-SCS semiconductor system and the Suss PM5 analytical probe station. The HER was carried out by using a two-electrode system to monitor the completeness of the PMMA coating on single and dual copper wires. As-prepared fibers and a platinum wire were used as working electrodes and counter electrode, respectively. Dilute sulfuric acid solution (0.5 mol L^{-1}) was used as the electrolyte. The electrochemical measurement was performed using the electrochemical workstation CHI 660E. All experiments were performed at room temperature.

Supporting Information

Supporting Information is available from the Wiley Online Library or from the author.

Acknowledgements

Conflict of Interest

The authors declare no conflict of interest.

Keywords

[1] a) J. W. Strutt, L. Rayleigh, *Proc. London Math. Soc.* **1878**, *10*, 4; b) L. Rayleigh, *Proc. R. Soc. London* **1979**, *29*, 71; c) J. Plateau, *Experimental and Theoretical Steady State of Liquids Subjected to Nothing but Molecular Forces*, Gauthiers-Villars, Paris, France **1873**.

[2] a) J. J. Kaufman, G. Tao, S. Shabahang, E. -H. Banaei, D. S. Deng, X. Liang, S. G. Johnson, Y. Fink, A. F. Abouraddy, *Nature* **2012**, *487*, 463; b) F. Gallaire, P.-T. Brun, *Philos. Trans. R. Soc., A* **2017**, *375*, 20160155.

[3] a) H. Song, R. F. Ismagilov, *J. Am. Chem. Soc.* **2003**, *125*, 14613; b) Y. Li, J. J. Suen, E. Prince, E. M. Larin, A. Klinkova, H. Thérien-Aubin, S. Zhu, B. Yang, A. S. Helmy, O. D. Lavrentovich, E. Kumacheva, *Nat. Commun.* **2016**, *7*, 12520; c) A. Gumennik, L. Wei, G. Lestoquoy, A. M. Stolyarov, X. Jia, P. H. Rekemeyer, M. J. Smith, X. Liang, B. J.-B. Grena, S. G. Johnson, S. Gradecak, A. F. Abouraddy, J. D. Joannopoulos, Y. Fink, *Nat. Commun.* **2013**, *4*, 2216.

[4] a) X. Tian, Y. Chen, Y. Zheng, H. Bai, L. Jiang, *Adv. Mater.* **2011**, *23*, 5486; b) H. Bai, J. Ju, Y. Zheng, L. Jiang, *Adv. Mater.* **2012**, *24*, 2786; c) H. Bai, R. Sun, J. Ju, X. Yao, Y. Zheng, L. Jiang, *Small* **2011**, *7*, 3429; d) Z. Liu, D. Qi, G. Hu, H. Wang, Y. Jiang, G. Chen, Y. Luo, X. J. Loh, B. Liedberg, X. Chen, *Adv. Mater.* **2018**, *30*, 1704229.

[5] L. Shang, F. Fu, Y. Cheng, Y. Yu, J. Wang, Z. Gu, Y. Zhao, *Small* **2017**, *13*, 1600286.

[6] a) S. Shabahang, J. J. Kaufman, D. S. Deng, A. F. Abouraddy, *Appl. Phys. Lett.* **2011**, *99*, 161909; b) H. Dong, N. Wang, L. Wang, H. Bai, J. Wu, Y. Zheng, Y. Zhao, L. Jiang, *ChemPhysChem* **2012**, *13*, 1153; c) Y.-J. Chiu, H.-F. Tseng, Y.-C. Lo, B.-H. Wu, J. Chen, *Macromol. Rapid Commun.* **2017**, *38*, 1600689.

[7] Y. Son, N. S. Martys, J. G. Hagedorn, K. B. Migler, *Macromolecules* **2003**, *36*, 5825.

[8] a) C. Duprat, S. Protiere, A. Y. Beebe, H. A. Stone, *Nature* **2012**, *482*, 510; b) S. Protiere, C. Duprat, H. A. Stone, *Soft Matter* **2013**, *9*, 271; c) A. Sauret, F. Boulogne, D. Cebron, E. Dressaire, H. A. Stone, *Soft Matter* **2015**, *11*, 4034.

[9] a) H. M. Princen, *J. Colloid Interface. Sci.* **1970**, *34*, 171; b) J. Bico, B. Roman, L. Moulin, A. Boudaoud, *Nature* **2004**, *432*, 690; c) H. Liu, S. Li, J. Zhai, H. Li, Q. Zheng, L. Jiang, D. Zhu, *Angew. Chem., Int. Ed.* **2004**, *43*, 1146.

[10] a) F. Boulogne, M. A. Fardin, S. Lerouge, L. Pauchard, F. Giorgiutti-Dauphine, *Soft Matter* **2013**, *9*, 7787; b) X. Liu, S. Shi, Y. Li, J. Forth, D. Wang, T. P. Russell, *Angew. Chem., Int. Ed.* **2017**, *56*, 12594; c) A. Alchalaby, R. Lwin, A. H. Al-Janabi, P. W. Trimby, S. C. Fleming, B. T. Kuhlmey, A. Argyros, *J. Lightwave Technol.* **2016**, *34*, 2198.

[11] a) Z. Shao, F. Vollrath, *Nature* **2002**, *418*, 741; b) A. R. Murphy, D. L. Kaplan, *J. Mater. Chem.* **2009**, *19*, 6443; c) G. H. Altman, F. Diaz, C. Jakuba, T. Calabro, R. L. Horan, J. Chen, H. Lu, J. Richmond, D. L. Kaplan, *Biomaterials* **2003**, *24*, 401; d) F. G. Omenetto, D. L. Kaplan, *Science* **2010**, *329*, 528.

[12] a) T. D. Sutherland, J. H. Young, S. Weisman, C. Y. Hayashi, D. J. Merritt, *Annu. Rev. Entomol.* **2010**, *55*, 171; b) D. N. Rockwood, R. C. Preda, T. Yücel, X. Wang, M. L. Lovett, D. L. Kaplan, *Nat. Protoc.* **2011**, *6*, 1612.

[13] Y. Zheng, H. Bai, Z. Huang, X. Tian, F.-Q. Nie, Y. Zhao, J. Zhai, L. Jiang, *Nature* **2010**, *463*, 640.

[14] M. Miura, Z. J. Pan, S. Aoyama, H. Morikawa, S. J. Mochizuki, *J. Seric. Sci. Jpn.* **1998**, *67*, 51.

[15] a) B. Taylor, *Philos. Trans. R. Soc. London* **2008**, *27*, 538; b) A. Ponomarenko, D. Quéré, C. Clanet, *J. Fluid Mech.* **2011**, *666*, 146.

[16] a) J. Li, X. Zhou, J. Li, L. Che, J. Yao, G. McHale, M. K. Chaudhury, Z. Wang, *Sci. Adv.* **2017**, *3*, eaao3530; b) P. Concus, R. Finn, *Proc. Natl. Acad. Sci. U.S.A.* **1969**, *63*, 292.

[17] B. Hu, Z. Duan, B. Xu, K. Zhang, Z. Tang, C. Lu, M. He, L. Jiang, H. Liu, *J. Am. Chem. Soc.* **2020**, *142*, 6111.

[18] C. Zhang, E. B. Charles, H. A. Peter, G. K. Konstantin, *J.R. Soc., Interface* **2018**, *5*, 171241.

[19] a) F. Brochard, *J. Chem. Phys.* **1986**, *84*, 4664; b) J. Y. Huang, Y.-C. Lo, J. J. Niu, A. Kushima, X. Qian, L. Zhong, S. X. Mao, J. Li, *Nat. Nanotechnol.* **2013**, *8*, 277.

[20] a) P. G. de Gennes, *Rev. Mod. Phys.* **1985**, *57*, 827; b) D. Bonn, J. Eggers, J. Indekeu, J. Meunier, E. Rolley, *Rev. Mod. Phys.* **2009**, *81*, 739.

[21] a) L. H. Tanner, *J. Phys.: D: Appl. Phys.* **1979**, *12*, 1473; b) M. N. Popescu, G. Oshanin, S. Dietrich, A. M. Cazabat, *J. Phys.: Condens. Matter* **2012**, *24*, 243102.

[22] H. Chen, P. Zhang, L. Zhang, H. Liu, Y. Jiang, D. Zhang, Z. Han, L. Jiang, *Nature* **2016**, *532*, 85.

[23] S. H. Davis, *J. Fluid Mech.* **1980**, *98*, 225.

[24] a) D. Langbein, *J. Fluid Mech.* **1990**, *213*, 251; b) L. A. Romero, F. G. Yost, *J. Fluid Mech.* **1996**, *322*, 109; c) R. V. Roy, L. W. Schwartz, *J. Fluid Mech.* **1999**, *391*, 293.

[25] P. G. de Gennes, F. Brochard-Wyart, D. Quéré, *Capillarity and Wetting Phenomena*, Springer, New York **2004**.

[26] a) L. Landau, B. Levich, *Acta Physicochim. URSS* **1942**, *17*, 42; b) B. V. Derjaguin, *Acta Physicochim. URSS* **1943**, *20*, 349.

[27] a) F. P. Bretherton, *J. Fluid Mech.* **1961**, *10*, 166; b) D. Quéré, *Annu. Rev. Fluid Mech.* **1999**, *31*, 347.

ADVANCED MATERIALS

Supporting Information

Bioinspired Anti-Plateau–Rayleigh-Instability on Dual Parallel Fibers

Pengwei Wang, Jiajia Zhou, Bojie Xu, Cong Lu, Qing'an Meng, and Huan Liu*

WILEY-VCH

Supporting Information

Bioinspired Anti-Plateau–Rayleigh Instability on Dual Parallel Fibers

Pengwei Wang,[#] Jiajia Zhou,[#] Bojie Xu, Cong Lu, Qing'an Meng, Huan Liu*

Key Laboratory of Bio-Inspired Smart Interfacial Science and Technology of Ministry of Education, School of Chemistry, Beijing Advanced Innovation Center for Biomedical Engineering, International Research Institute for Multidisciplinary Science, Beihang University, Beijing, 100191, P. R. China

E-mail: liuh@buaa.edu.cn

[#] These two authors contributed equally.

1. SEM images of the nylon fibers.
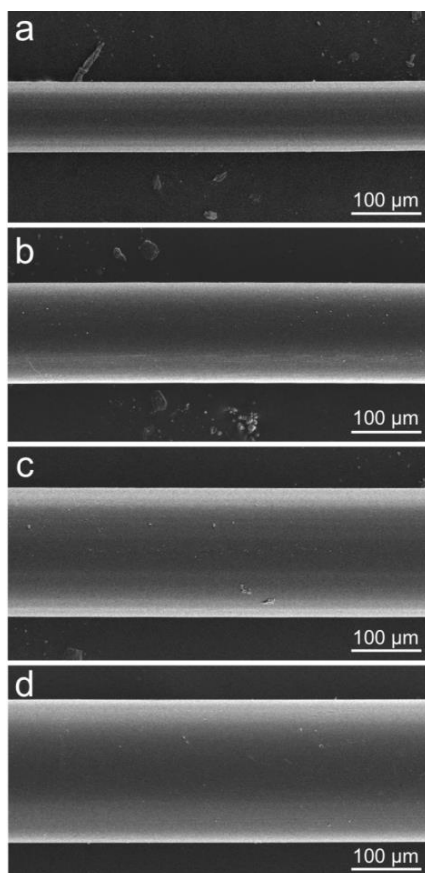
Figure S1. (a) 2b = 100 μm. (b) 2b = 130 μm. (c) 2b = 180 μm. (d) 2b = 200 μm.

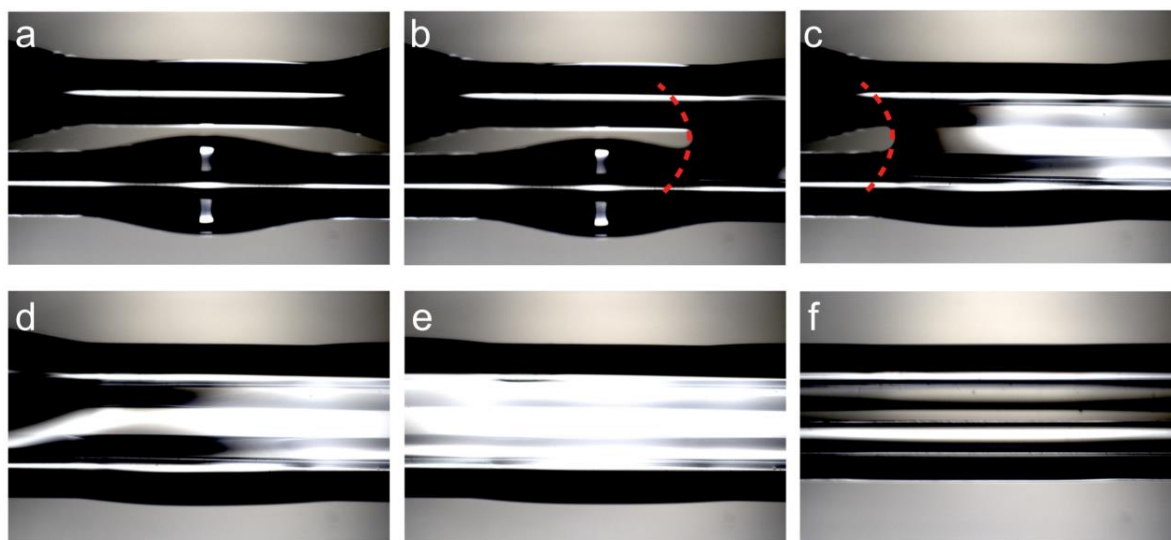2. Dynamic approaching process of two fibers.

Figure S2. The fibers are surrounded with periodic dislocation corresponding droplets.

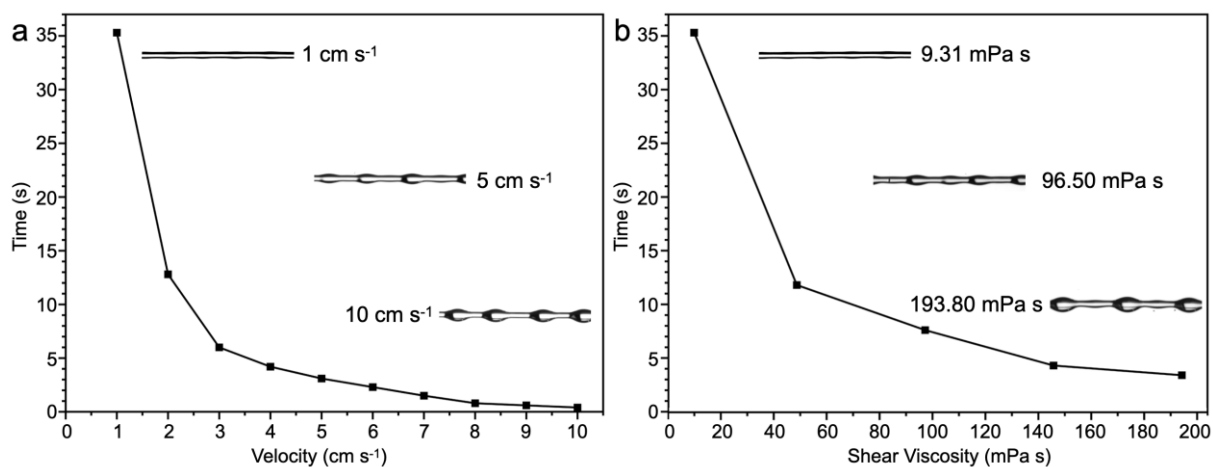3. The time of the PRI happening on the single fiber.

Figure S3. (a) The time of the PRI happening when the single nylon fiber was pulled out from silicon oils with same viscosity at the different velocity. The insets corresponding to the indicated velocity illustrate the final states of the liquid film. (b) The time of the PRI happening when the single nylon fiber was pulled out from silicon oils with different viscosity at the same velocity. The insets corresponding to the indicated viscosity illustrate the final states of the liquid film.

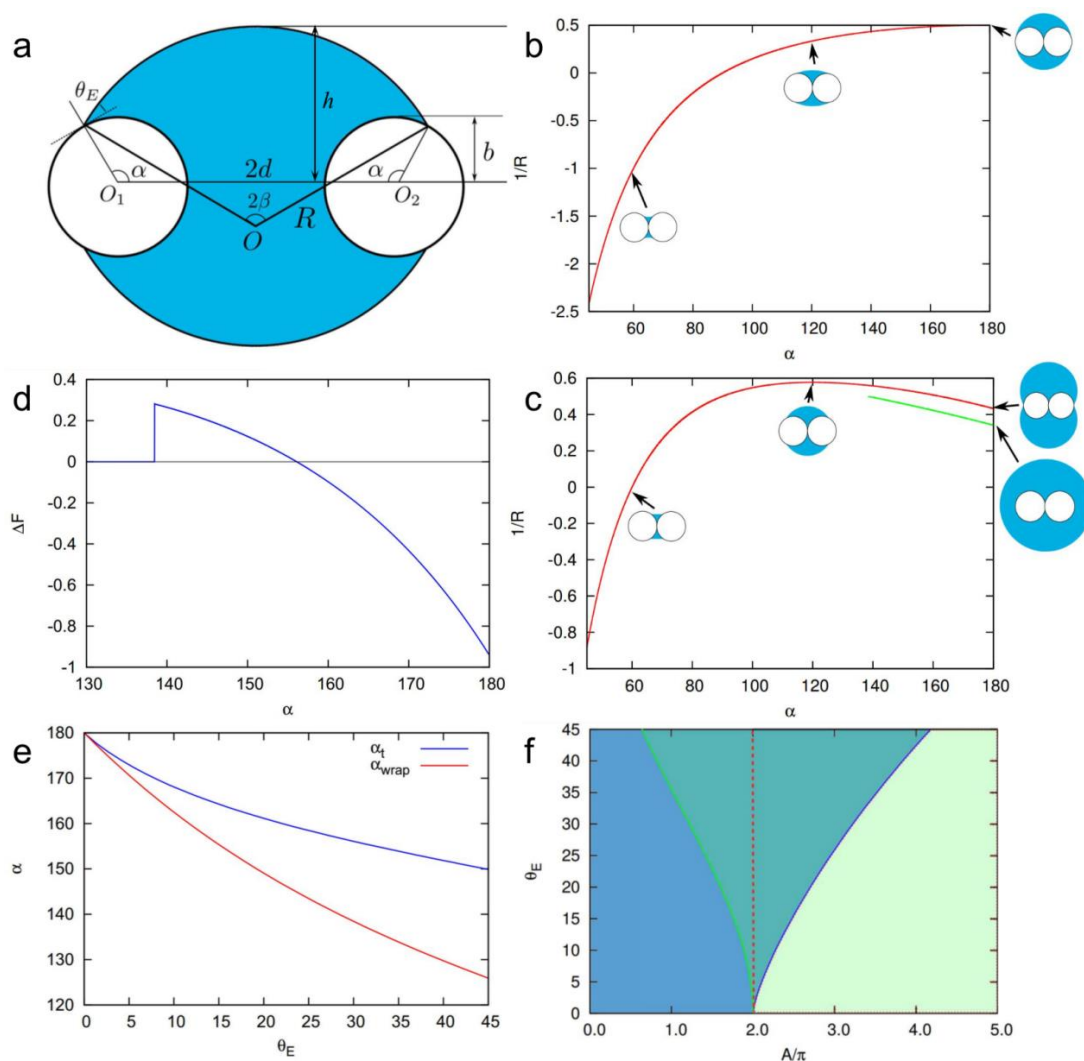4. Theoretical analysis of the liquid stability on the dual parallel fibers.

Figure S4. (a) The cross-section of the two fibers covered by the fluid, where b is the radius of the fiber, $2d$ is the distance between fibers, θ_E is the liquid-fiber contact angle, α is the wrapping angle, R is the radius of curvature, and A is the cross-sectional area of the liquid film. (b) The curvature for the case $d = 0$, $\theta_E = 0°$. (c) The curvature for the case $d = 0$, $\theta_E = 30°$. (d) The free energy difference for the case $d = 0$, $\theta_E = 30°$. (e) The two angles α_{wrap} and α_t as a function of θ_E for $d = 0$. (f) Phase diagram for $d = 0$. The x-axis is the fluid area divided by π (A/π), and the y-axis is the contact angle θ_E.

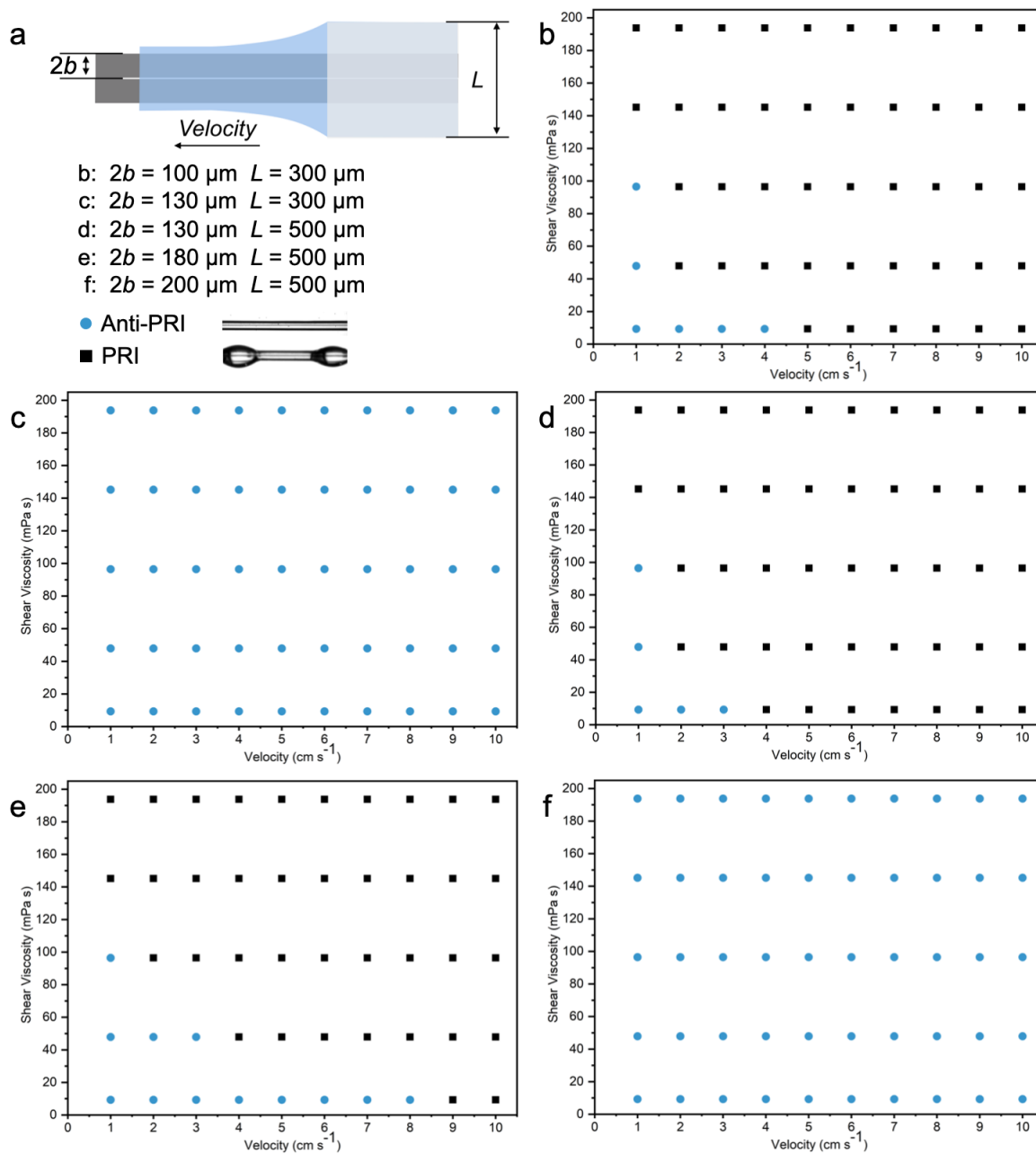5. Parallel nylon fibers pulled out from silicone oils.

Figure S5. (a) Diagrammatic sketch of the fluid coating processes of the parallel nylon fibers. (b-f) Maps of the PRI happening in different experimental conditions (blue circles: the PRI is overcome; black squares: the PRI happens). (b) 2b = 100 μm, L = 300 μm. (c) 2b = 130 μm, L = 300 μm. (d) 2b = 130 μm, L = 500 μm. (e) 2b = 180 μm, L = 500 μm. (f) 2b = 200 μm, L = 500 μm.

6. The final states of the liquid film in different experimental conditions.

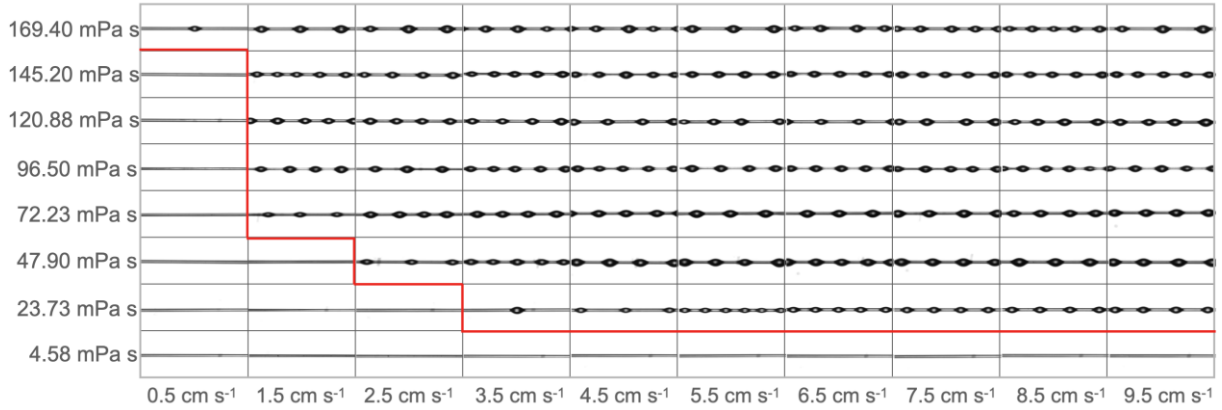Figure S6. The parallel nylon fibers with 100 μm diameter were pulled out from the silicon oils with different viscosity though capillary glass tube with 500 μm internal diameter.

Supplementary Text: Stability analysis of the liquid film on dual parallel fibers.

We consider two identical fibers of radius b and their axes located at O_{1z} and O_{2z}. The separation between the two fibers is $2d$ (surface to surface distance) (Figure S4a). There are actually two separate cases. One is when the fluid has a large volume so it can form a big cylinder which covers both fibers. The other one is when the amount of fluid is less. Due to the constant Laplace pressure, the fluid surfaces are parts of a circle with a radius of R. We will discuss the later case first, because the first one is much simpler. The details of the derivation can be found in Ref. (37).

For fixed set parameters $\{b, d, \theta_E\}$ (θ_E being the contact angle), the fluid shape can be characterized by one parameter 2α, which is the open angle of the fluid/fiber interface. We scale all length to the fiber radius b. The fluid surface curvature is given by

$$\tilde{R} = \frac{R}{b} = -\frac{1-\cos\alpha + \tilde{d}}{\cos(\alpha + \theta_E)}. \tag{1}$$

The radius is positive if the interface is convex when looking from the fluid to the gas phase. Figure S4b and S4c show the curvature $1/R$ as a function of α.

The open angle 2β is given by

$$\beta = \begin{cases} \dfrac{\pi}{2} - \alpha - \theta_E & \alpha + \theta_E < \dfrac{\pi}{2} \\ \alpha + \theta_E - \dfrac{\pi}{2} & \alpha + \theta_E \geq \dfrac{\pi}{2} \end{cases}$$

(2)

The area of the fluid cross-section is

$$\tilde{A} = \frac{A}{b^2} = 4\left(1 - \cos\alpha + \tilde{d}\right)\sin\alpha - 2\left(\alpha - \sin\alpha\cos\alpha\right)$$
$$-2\tilde{R}^2\left[\frac{\pi}{2} - \alpha - \theta_E - \sin\left(\alpha + \theta_E\right)\cos\left(\alpha + \theta_E\right)\right]$$

(3)

The height of the fluid is

$$\tilde{h} = \sin\alpha + \tilde{R}\left[1 - \cos\left(\alpha + \theta_E - \frac{\pi}{2}\right)\right].$$

(4)

When fluid volume is large enough, there are two possible configurations. One is the situation discussed above, when part of the fiber surface is exposed to the air; the other one is a full circle with the same fluid volume. The radius of the full circle is given by

$$\pi\tilde{R}^2 = A + 2\pi b^2, \quad \text{only if } \tilde{R} > 2b + d.$$

(5)

For the case shown in Figure S4b ($d = 0$, $\theta_E = 0°$), the condition cannot be satisfied. For the case shown in Figure S4c ($d = 0$, $\theta_E = 30°$), the fluid may take either configurations when $\alpha > 138°$. We denote this angle as α_{warp}. Once the $\alpha > \alpha_{warp}$, which configuration is chosen will depend on the free energy. For the case of one full circle per unit length in z-direction is

$$F_1 = 2\pi R'\gamma + 4\pi b\gamma_{SL}.$$

(6)

For the case with fiber/air interface, the free energy is

$$F_2 = 4\beta R\gamma + 4\left(\pi - \alpha\right)b\gamma_{SV} + 4\alpha b\gamma_{SL}.$$

(7)

The difference is

$$\Delta F = F_1 - F_2 = \left(2\pi R' - 4\beta R\right)\gamma + 4\left(\pi - \alpha\right)b\left(\gamma_{SL} - \gamma_{SV}\right)$$
$$\frac{\Delta F}{\gamma} = \left(2\pi R' - 4\beta R\right) - 4\left(\pi - \alpha\right)b\cos\theta_E,$$

(8)

where we have used Young's equation $\gamma_{SV} = \gamma_{SL} + \gamma \cos \theta_E$. The system will take the full

circle configuration only if $\Delta F < 0$. Figure S4d shows the free energy difference for the case

shown in Figure S4c. The full circle configuration becomes more stable when α exceeds around

155°. We denote the transition angle as α_t.

Figure S4e shows the two angles α_{wrap} and α_t as a function of the contact angle θ_E for the

case $d = 0$. It can be viewed as a phase diagram. Here we replot the figure using A instead of α,

which is shown in Figure S4f. In the region left to the blue line, the configuration with two

partial circles are stable; while on the right to the blue line, the full circle configration is more

stable. The red line characterizes the appearance of the full circle configuration. In between the

red and blue line, both configurations are possible, but the full circle is unstable. The green line

is related to the PRI, which will be discussed later.

Suppose the flow velocity in the cross-section is much less than the velocity along the z-

axis. The Stokes equation gives

$$\eta \left(\frac{\partial^2 u}{\partial x^2} + \frac{\partial^2 u}{\partial y^2} \right) - \frac{\partial p}{\partial z} = 0.$$

$$(9)$$

For one-dimensional flow, the flow rate $Q = \int dx dy u$ is related to the pressure gradient by

$$-\mu \frac{\partial p}{\partial z} = Q,$$

$$(10)$$

where μ is the fluid mobility.

The conservation of the fluid volume gives

$$\frac{\partial A}{\partial t} = -\frac{\partial Q}{\partial z}.$$

$$(11)$$

Substitute Eq. (10) into (11)

$$\frac{\partial}{\partial z} \left(\mu \frac{\partial p}{\partial z} \right) = \frac{\partial A}{\partial t},$$

$$(12)$$

which can be linearized to

$$\mu_0 \frac{\partial^2 \delta p}{\partial z^2} = \frac{\partial \delta A}{\partial t},$$

(13)

where μ_0 is given at the unperturbed reference state.

We now consider the local variation of α with fixed contact angle θ_E

$$\alpha = \alpha_0 + \delta\alpha = \alpha_0 + \epsilon_\alpha e^{ikz+t/\tau}.$$

(14)

We need the local Laplace pressure in the fluid. The curvature in the cross-section is

$$\delta c_\perp = -\frac{\delta R}{R_0^2} = -\frac{1}{R_0^2}\frac{\partial R}{\partial \alpha}\bigg|_{\alpha_0} \epsilon_\alpha e^{ikz+t/\tau}.$$

(15)

We approximate the variation of the initial zero normal curvature c by the second derivative of the height variation δh of the center line

$$\delta c_\parallel = -\frac{\partial^2 \delta h}{\partial z^2} = \frac{\partial h}{\partial \alpha}\bigg|_{\alpha_0} k^2 \epsilon_\alpha e^{ikz+t/\tau}.$$

(16)

The variation of the Laplace pressure is

$$\delta p = \gamma(\delta c_\perp + \delta c_\parallel) = \gamma\left[-\frac{1}{R_0^2}\frac{\partial R}{\partial \alpha}\bigg|_{\alpha_0} + \frac{\partial h}{\partial \alpha}\bigg|_{\alpha_0} k^2\right]\epsilon_\alpha e^{ikz+t/\tau}.$$

(17)

The LHS of Eq. (13) is

$$\frac{1}{\xi_0}\frac{\partial^2 \delta p}{\partial z^2} = \gamma\mu_0\left[\frac{1}{R_0^2}\frac{\partial R}{\partial \alpha}\bigg|_{\alpha_0} k^2 - \frac{\partial h}{\partial \alpha}\bigg|_{\alpha_0} k^4\right]\epsilon_\alpha e^{ikz+t/\tau}.$$

(18)

The RHS of Eq. (13) is

$$\frac{\partial \delta A}{\partial t} = \frac{\partial A}{\partial \alpha}\bigg|_{\alpha_0} \tau^{-1}\epsilon_\alpha e^{ikz+t/\tau}.$$

(19)

Finally, we reach the growth rate

$$\tau^{-1} = \gamma\mu_0 \frac{\left[\frac{1}{R_0^2}\frac{\partial R}{\partial \alpha}\bigg|_{\alpha_0} k^2 - \frac{\partial h}{\partial \alpha}\bigg|_{\alpha_0} k^4\right]}{\frac{\partial A}{\partial \alpha}\bigg|_{\alpha_0}}$$

$$= B\frac{\gamma A}{\eta b^3} \frac{\left[\frac{1}{\tilde{R}_0^2}\frac{\partial \tilde{R}}{\partial \alpha}\bigg|_{\alpha_0} (kb)^2 - \frac{\partial \tilde{h}}{\partial \alpha}\bigg|_{\alpha_0} (kb)^4\right]}{\frac{\partial \tilde{A}}{\partial \alpha}\bigg|_{\alpha_0}}$$

(20)

8

The appearance of the instability depends on the sign of the factor in front of $(kb)^2$ term in Eq. (20).

$$\left.\frac{\partial \tilde{R}}{\partial \alpha}\right|_{\alpha_0} > 0, \quad \Rightarrow \quad \alpha > \pi - 2\theta_E.$$

(21)

If this condition is satisfied, the fast mode has a wavenumber

$$\left(k^* b\right)^2 = \frac{\dfrac{1}{\tilde{R}_0^2}\left.\dfrac{\partial \tilde{R}}{\partial \alpha}\right|_{\alpha_0}}{2\left.\dfrac{\partial \tilde{h}}{\partial \alpha}\right|_{\alpha_0}}.$$

(22)

The fastest growth rate is

$$\left(\tau^*\right)^{-1} = B\frac{\gamma A}{4\eta b^3}\frac{\left(\dfrac{1}{\tilde{R}_0^2}\left.\dfrac{\partial \tilde{R}}{\partial \alpha}\right|_{\alpha_0}\right)^2}{\left.\dfrac{\partial \tilde{A}}{\partial \alpha}\right|_{\alpha_0}\left.\dfrac{\partial \tilde{h}}{\partial \alpha}\right|_{\alpha_0}}.$$

(23)

For the fully wetted case, $\theta_E = 0^\circ$, the stable condition becomes

$$\alpha \leq \pi, \quad \Rightarrow \quad A \leq 2\pi b^2$$

(24)